Hindawi
International Journal of Energy Research
Volume 2024, Article ID 9935893, 13 pages
https://doi.org/10.1155/2024/9935893

Research Article

In-Depth Analysis on the Fabry-Perot Effect of $Cs_2AgBiBr_6$ Double Perovskite-Based Solar Cells via Optical Path Length Modulation

Kyeong-Ho Seo, Junhao Feng, and Jin-Hyuk Bae

School of Electronic and Electrical Engineering, Kyungpook National University, 80 Daehakro, Bukgu, Daegu 702-701, Republic of Korea

Correspondence should be addressed to Jin-Hyuk Bae; jhbae@ee.knu.ac.kr

Received 8 August 2023; Revised 25 November 2023; Accepted 12 December 2023; Published 5 February 2024

Academic Editor: Muhammad Ahsan Saeed

Herein, the Fabry-Perot (F-P) interference of cesium silver bismuth bromide ($Cs_2AgBiBr_6$) double perovskite solar cells has been analyzed by modulating the optical path length of each layer step by step using the finite-difference time-domain (FDTD) method. The study was performed pass through three main steps. In step 1, for the fluorine-doped tin oxide (FTO)/$Cs_2AgBiBr_6$ double perovskite/gold (Au) architecture, we increased the absorption layer thickness from 150 to 600 nm at intervals of 150 nm and then predicted the optical performance including the absorption and reflection. In step 2, titanium dioxide (TiO_2) layer was added between FTO electrode and $Cs_2AgBiBr_6$ double perovskite and then scaled from 20 to 200 nm at intervals of 20 nm. In the analysis process, short-circuit current density (J_{sc}) repeatedly fell and rose as the TiO_2 layer thickness increased, and when TiO_2 layer thickness is 100 nm, J_{sc} showed the highest value of 13.91 mA/cm^2. In step 3, by applying a spiro-OMeTAD layer between the $Cs_2AgBiBr_6$ double perovskite absorption layer and Au electrode, the J_{sc} showed a continuous increase with slight decrease as the spiro-OMeTAD layer thickness increased from 110 to 200 nm, and when the spiro-OMeTAD layer thickness was 200 nm, $J_{sc}$was calculated as 14.57 mA/cm^2, which is the highest value in the range. In the case of the optimal condition of full structure device, the Fabry-Perot resonance peaks were discovered at 477, 520, 572, 659, and 778 nm five wavelength regions, and the influence of the Fabry-Perot resonance on the generation rate inside the absorption layer on the 520, 572, and 659 nm monochromatic wavelength light was analyzed according to the position in the device. Our study approaches the $Cs_2AgBiBr_6$ double perovskite solar cell from an F-P cavity perspective and shows the light trapping phenomenon of the device according to the optical path length modulation.

1. Introduction

Over the past few decades, fossil fuels are a core resource in human society, and their use is increasing dramatically in the world's population. However, fossil fuels tend to be depleted over time, and in preparation for this, there is a need to supplement the new alternative energy. Alternative energy sources including solar, wind, hydro, and geothermal energy play an important role in supplying electricity to future generation. Among them, the solar energy is abundant, cost-free, and ecofriendly renewable energy and is considered to be a promising alternative energy currently being researched [1–3]. In a worldwide, the global market for solar systems is rapidly growing, with solar systems currently accounting for 26.2% of total global energy generated, with solar systems accounting for 2.4% [1]. The growth of solar power generation systems is expected to increase and develop as the years go by.

Organic–inorganic lead halide perovskite solar cells (PSCs) have attracted significant attention as new-generation photovoltaics due to their improved power conversion efficiency (PCE) comparable to photovoltaic materials such as silicon (Si) and copper indium gallium selenide [4–6]. Park et al. recently discovered a new method and principle for

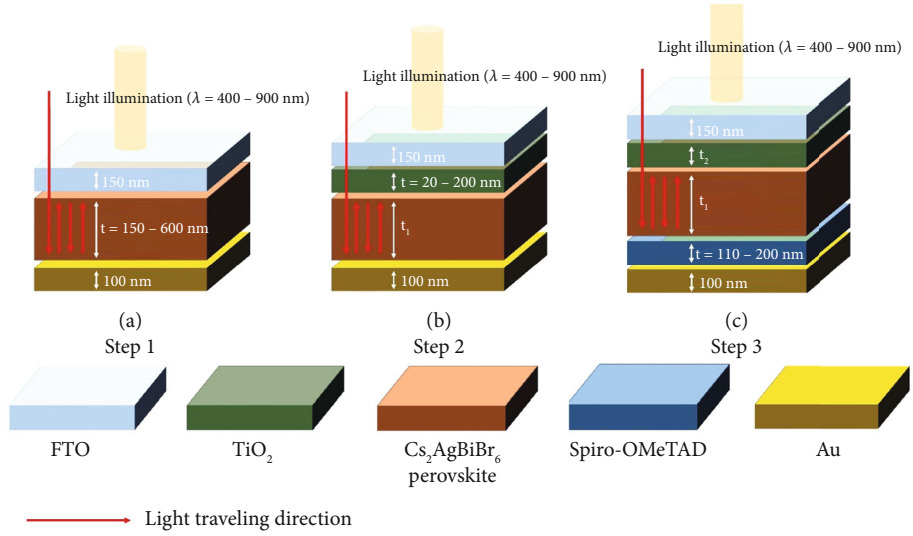

FIGURE 1: Schematics of the $Cs_2AgBiBr_6$ perovskite-based solar cell with FP cavity mode. Step 1 indicates the FTO/$Cs_2AgBiBr_6$ perovskite/Au structure, step 2 indicates the FTO/TiO_2/$Cs_2AgBiBr_6$ perovskite/Au structure, and step 3 indicates the FTO/TiO_2/$Cs_2AgBiBr_6$ perovskite/spiro-OMeTAD/Au structure. A red arrow symbol indicates the light traveling direction.

controlling the crystallinity of a perovskite photoactive layer and achieved the highest PCE of 26.08. Nevertheless, the commercialization of the typical $APb^{2+}X_3$ ($A = MA^+$ (CH_3NH_{3+}), FA^+ ($CH(NH_2)^{2+}$), Cs+, or mixed A-cations; $X = I^-$, Br^-, or Cl^-) perovskite structure has a problem of the limitation due to the Pb^{2+} toxicity [7, 8].

Recently, research to replace Pb^{2+}-based perovskites with Pb^{2+}-free materials has been actively performed. One of the ways is to replace two divalent Pb^{2+} ions with one monovalent M^+ and one trivalent M^{3+} ion, forming an $A_2M^+M^{3+}X_6$ double perovskite structure [8, 9]. Among this class of compounds, $Cs_2AgBiBr_6$ double perovskite has attracted much attention due to its high stability, low toxicity, and high sensitivity in the UV–blue wavelength region corresponding to the bandgap (≈1.9 eV). [10–12]. Specifically, $Cs_2AgBiBr_6$ perovskite is air-stable for about 2 weeks, which is longer than the class of $ASnI_3$ perovskite, one of the representative perovskite materials [13]. Moreover, bismuth- (Bi-) based perovskite, which is one of the attractive nontoxic perovskites, is one of the group 15 elements like Sb, with better chemical stability as compared to Pb-based perovskites. Besides, $Cs_2AgBiBr_6$ double perovskite has significant advantages of higher external quantum efficiency (≈60%), longer carrier lifetime (≈1 μs), and more moderate charge carrier mobility than other Pb^{2+}-free perovskites [11, 14]. However, its light-harvesting ability is very poor due to its large direct bandgap, which leads to a very low short-circuit current density (J_{sc}), resulting in very low PCE (≈6%; Ravi et al., 2018) for $Cs_2AgBiBr_6$ double PSC commercialization. To the best of our knowledge, solar cells using $Cs_2AgBiBr_6$ double perovskite are recent research, and little information is available compared to other perovskites.

To overcome the low PCE of $Cs_2AgBiBr_6$ double perovskite-based solar cells, the most important research is to improve the poor light harvesting of $Cs_2AgBiBr_6$ double perovskite due to the large indirect band gap. To date, many studies have been conducted to improve the light-harvesting capability and optoelectronic properties of photovoltaics. One of the representative methods is to utilize light trapping technology [15–17]. Light trapping is a strategy for controlling photon absorption by extending the optical path length (OPL) [17, 18]. One of the representative light trapping strategies is metallization for electronic applications. Embedding metallic nanoparticles such as gold (Au), silver (Ag), or copper (Cu) in the active layer plays a crucial role in reducing exciton quenching and cell resistance, significantly improving PCE [19, 20]. Localized surface plasmon resonance (LSPR), in which the surface of a metal nanostructure glows when exposed to light, utilizes the light trapping for metalized solar cell with various plasmonic structures, contributing to enhance the light absorption [21–23]. By embedding these plasmonic nanostructures in solar cells and illuminating them, the light-harvesting capability can be improved using the localized surface plasmon resonance principle, which improves light scattering efficiency [24, 25].

Another strategy to improve light trapping in solar cell is to use the Fabry-Perot (F-P) effect. The F-P cavity is a structure in which two reflectors with high reflectance are placed in parallel at a certain distance, enhancing the optical absorption [26–29]. The F-P cavity is used to analyze the interference phenomenon of light acting between reflecting mirrors [30–32]. Light waves generated in the cavity and reflected light waves cause constructive and destructive interference; only light waves of a specific wavelength remain, and all others are canceled out, allowing only specific wavelengths of light to pass through selectively and appear as output. As a result, the optical path length (OPL) of the cell increases, and the light absorption ability is enhanced [33, 34]. Djurić and Jokić studied about F-P cavity mode PSC with p-i-n device structure, then investigated the maximum efficiency of PSC using the theoretical backgrounds, and explained the interference effects of PSC

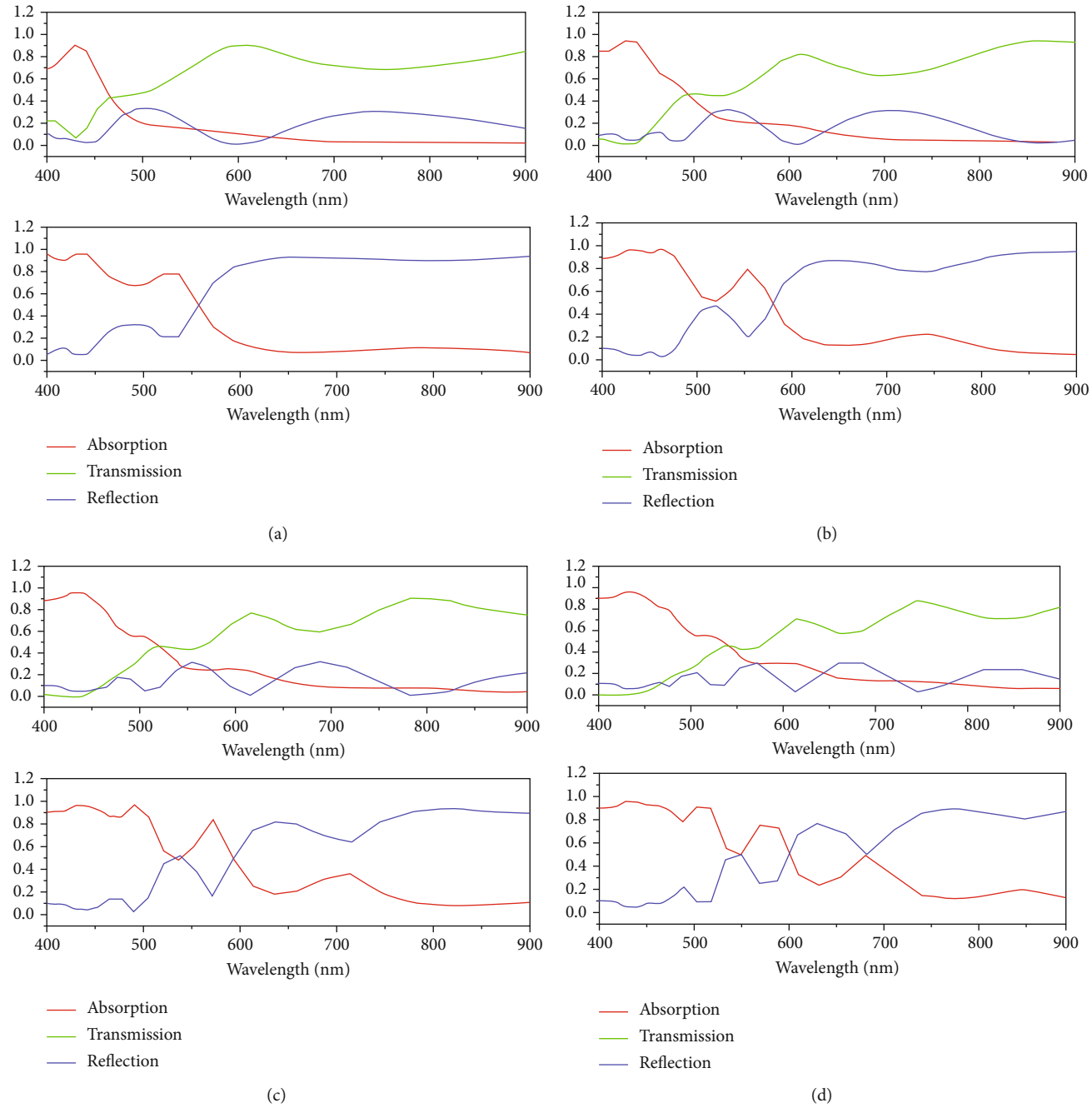

Figure 2: Optical performance of $Cs_2AgBiBr_6$ double perovskite-based architecture with different absorption layer thicknesses under solar light plane wave illumination. Each top data indicates optical performance without Au electrode, and each bottom data indicates optical performance with Au electrode. (a) 150 nm, (b) 300 nm, (c) 450 nm, and (d) 600 nm.

structure represented by a F-P resonator [29]. In conclusion, analysis of the F-P effect within the $Cs_2AgBiBr_6$ double perovskite with large indirect band gap-based solar cell is particularly significant for enhancing the optical absorption and light trapping.

Based on the foregoing, this study focused on the optical–electrical properties based on the F-P effect of $Cs_2AgBiBr_6$ PSCs with a fluorine-doped tin oxide (FTO) top electrode and a gold (Au) bottom electrode [35, 36]. We regarded the FTO/$Cs_2AgBiBr_6$ perovskite/Au architecture as an FP cavity and analyzed the electromagnetic wave propagation in the device via the finite-difference time-domain (FDTD) method [22, 37]. In 2023, Pritom et al. designed a Si solar cell with parabola moth-eye antireflection layer and used FDTD simulation to investigate the F-P resonance occurring in the device [38]. To construct the n-i-p structure solar cell, we formed the titanium dioxide (TiO_2) and spiro-OMeTAD as an electron transport layer and a hole transport layer, respectively, and then investigated the optoelectronic properties, step by step. TiO_2 is the common ETL material which is used in PSC with its suitable energy match and good transparency, while spiro-OMeTAD is the common

Table 1: Average optical performance of W/O and W/ Au electrode until 660 nm continuous wavelength light.

Absorption layer thickness (nm)	Average absorption		Average transmission		Average reflection	
	W/O Au electrode	W/ Au electrode	W/O Au electrode	W/ Au electrode	W/O Au electrode	W/ Au electrode
150	0.16	0.32	0.65	—	0.19	0.68
300	0.23	0.38	0.62	—	0.15	0.62
450	0.28	0.42	0.57	—	0.14	0.58
600	0.32	0.46	0.53	—	0.15	0.54

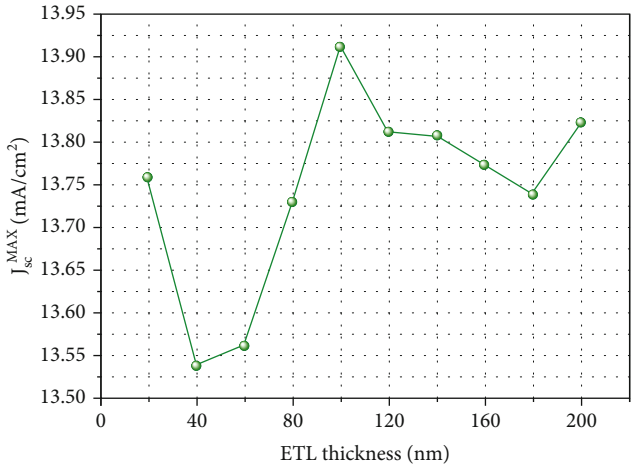

Figure 3: Short-circuit current density of FTO/TiO_2/$Cs_2AgBiBr_6$ perovskite/Au device with different ETL layer thicknesses.

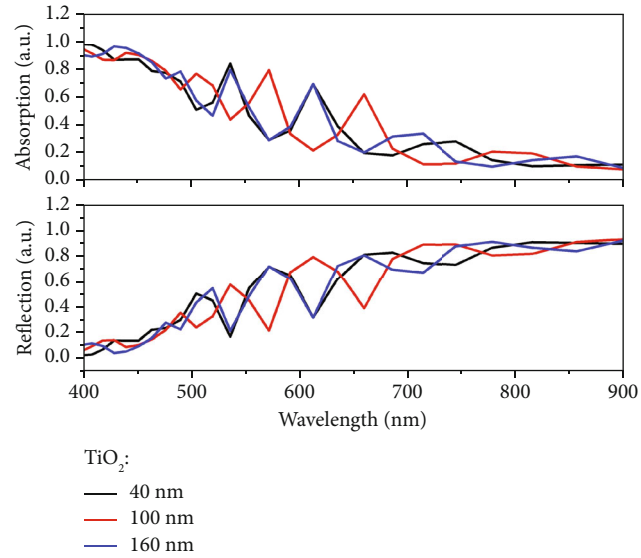

Figure 4: Optical performance of absorption layer within $Cs_2AgBiBr_6$ double perovskite-based architecture with different TiO_2 layer thicknesses under solar light plane wave illumination. Top data indicate the absorption of designed architecture, and bottom data indicate the reflection of designed architecture.

HTL material with the matching energy level and nonreactive properties between spiro-OMeTAD and the perovskite layer [39, 40]. The OPL was modulated by scaling the layer thickness while the refractive index value at each light wavelength was fixed [41]. By scaling the thickness of $Cs_2AgBiBr_6$, TiO_2, and spiro-OMeTAD layer, optimal OPL conditions of the device and resulting electrical performance have been calculated, and optimized device conditions and the resulting F-P resonance at a function of wavelength were investigated via FDTD simulation.

2. Simulation Procedure

We used the two-dimensional FDTD method to analyze the electromagnetic wave propagation mechanism in a user-defined medium-based architecture. The FDTD method is a methodology that solves Maxwell's equations in the time domain, considers light as an electromagnetic wave, and analyzes it from a wave optical perspective with state-of-the-art technology. Therefore, the FDTD technique provides researchers with optimal optical modeling conditions in nanophotonics research. This method, devised by Kane Yee, simulates the interaction of electromagnetic waves in a medium by solving Maxwell's equation [42]. Bader and Saghaei used this FDTD solution to analyze the tunability of the metamaterial absorbers under the terahertz spectrum corresponding to 0.2–20 THz [43]. In addition, Islam et al. [44] numerically studied the absorption and reflection of various optical metamaterials nanoabsorbers with the aim of improving the refractive index sensitivity sensitivity using the FDTD domain [44]. Lumerical FDTD solution software was utilized, which has a built-in technology computer-aided designing (TCAD) module for drawing the solar cell structure. Figure S1 shows the refractive index of materials which are used in the study. The refractive index of Au was based on cyclic redundancy check (CRC) data embedded in the software. We illustrate the simulation procedure step by step, as depicted in Figure 1. Referring to Islam et al., the optimal PCE of the solar cell appeared when the thickness of $Cs_2AgBiBr_6$ perovskite layer was 600 nm via simulation, and we analyzed the $Cs_2AgBiBr_6$ perovskite solar cell by scaling the absorption layer thickness from 150 to 600 nm with a 150 nm interval [44]. Next, in step 2, we designed the FTO/TiO_2/optimal $Cs_2AgBiBr_6$ perovskite (t_1)/Au-based architecture and investigated the electrical performance as a function of TiO_2 layer thickness and optical performance. The TiO_2 layer thickness was scaled from 20 to 200 nm with a 20 nm interval. We considered the range referred to other theoretical and experimental results in the literature; a lower-thickness TiO_2 layer (approximately 60 nm or less) calculates a relatively low J_{sc} and shows a continuous decreasing tendency, while a high-thickness TiO_2 layer (approximately 100 nm or more)

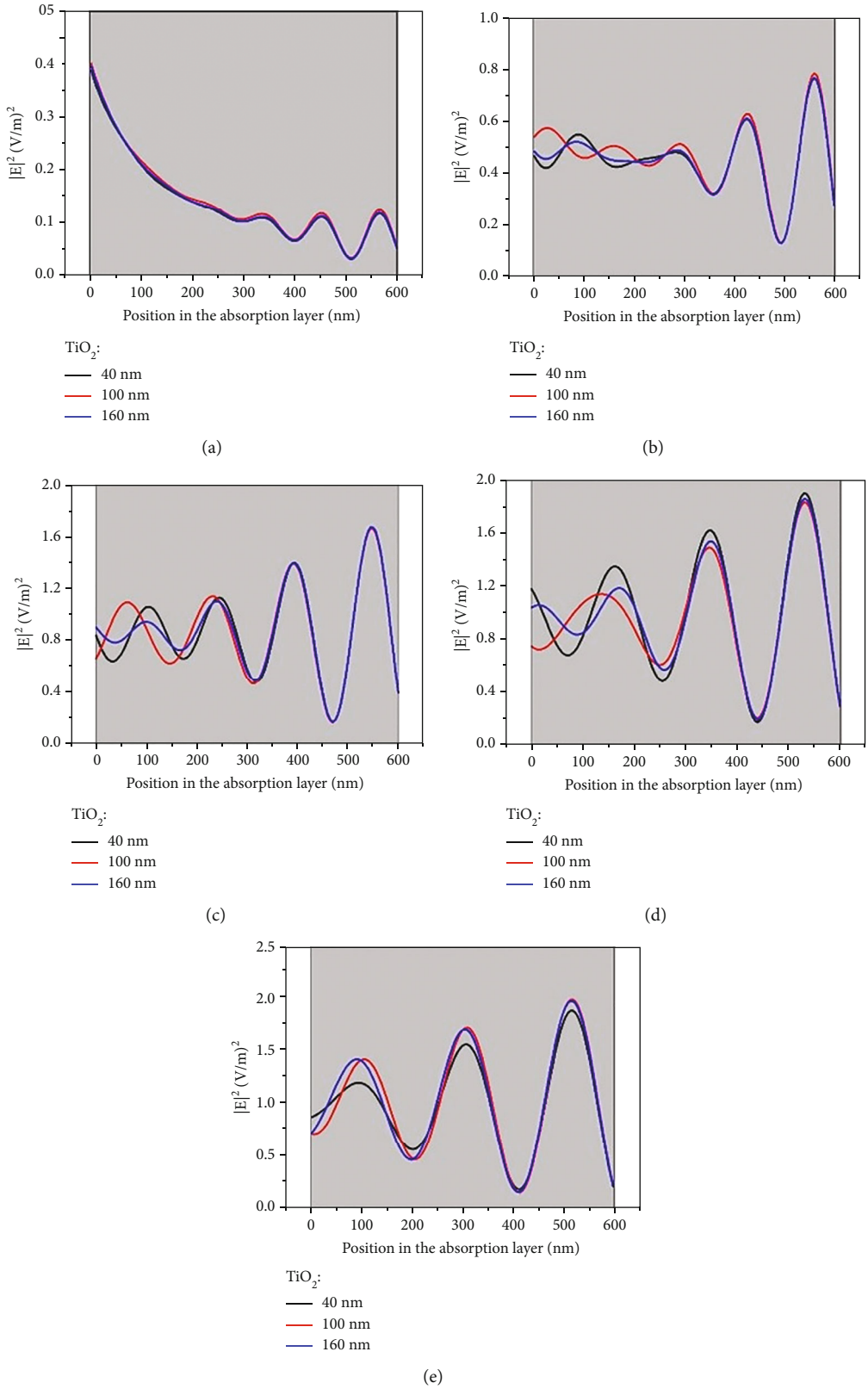

Figure 5: Spatial distribution of $|E|^2$ of absorption layer within $Cs_2AgBiBr_6$ double perovskite-based architecture with different TiO_2 layer thicknesses under solar light plane wave illumination. (a) Under 400–500 nm wavelength light illumination. (b) Under 500–600 nm. (c) Under 600–700 nm. (d) Under 700–800 nm. (e) Under 800–900 nm. The black, red, and blue spectra indicate the $|E|^2$ of the $Cs_2AgBiBr_6$ double perovskite-based architecture with 40 nm, 100 nm, and 160 nm thickness of TiO_2 layer, respectively.

Table 2: Average $|E|^2$ of the designed architecture with different TiO2 layer thicknesses. Units are unified as $(V/m)^2$.

TiO_2 layer thickness (nm)	Wavelength regime (nm)				
	400–500	500–600	600–700	700–800	800–900
40	0.138	0.454	0.884	0.993	1.006
100	0.143	0.472	0.892	0.961	1.048
160	0.14	0.456	0.891	0.985	1.053

calculates a high J_{sc}[45, 46]. This result is expected to be useful data for forming compact TiO_2 or mesoporous TiO_2 layers when fabricating real $Cs_2AgBiBr_6$ double perovskite solar cell. Finally, in step 3, it designed the FTO/optimal TiO_2 (t_2)/optimal $Cs_2AgBiBr_6$ perovskite (t_1)/spiro-OMeTAD/Au-based full structure device and then investigated the electrical performance as a function of TiO_2 layer thickness and optical performance. The spiro-OMeTAD layer was scaled from 110 to 200 nm with a 10 nm interval, considering the less recombination or other performance such as reproducibility in real fabrication [47]. A red arrow symbols indicate the light traveling direction, which indicates that light is repeatedly reflected between two electrodes.

Two-dimensional FDTD was set to run the simulation, and the simulation time and temperature were set to 1000 fs and 300 K, respectively. In the mesh setting, the mesh type was set to auto-nonuniform, and mesh accuracy was set to 4, considering speed, memory requirements, and economy of time. The boundary condition of all simulation steps was set with a periodic boundary condition along the x-axis, allowing for the calculation of the response of the entire system to the one-unit cell. The perfectly matched layer, which provides the zero-reflection coefficient for all incident angles of light, was set along the y-axis to avoid the parasitic reflection. By setting the FDTD according to these conditions, we were able to perform the rigorous modeling with an appropriate trade-off between fast and accuracy using mathematical algorithms such as Maxwell's equations even in complexly designed device structures.

3. Mathematical Algorithm

3.1. Finite-Difference Time-Domain Modeling Algorithm. P_{abs} can be calculated from the divergence of the Poynting vector and then converted into a more numerically stable form as

$$P_{abs} = -0.5\omega|E|^2 \text{imag}(\varepsilon), \tag{1}$$

where ω represents the angular frequency, and imag (ε) presents the imaginary part of permittivity. Assuming that all electron–hole pairs contribute to photocurrent, the J_{sc} can be calculated by

$$J_{sc} = e\int \frac{\lambda}{hc} \text{QE}(\lambda) I_{AM1.5G}(\lambda) d\lambda, \tag{2}$$

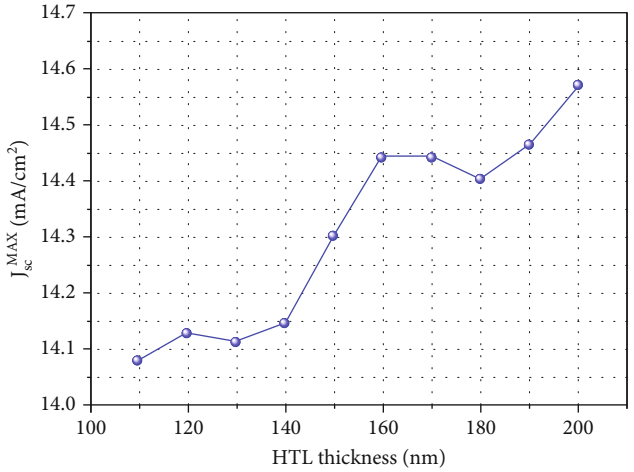

Figure 6: Short-circuit current density of FTO/TiO_2/$Cs_2AgBiBr_6$ perovskite/Au device with different HTL layer thicknesses.

where e represents the electron charge, QE(λ) denotes quantum efficiency, and $I_{AM1.5G}(\lambda)$ denotes a solar spectrum.

3.2. Fabry-Perot Wavelength-Dependent Power Transmission and Reflection. Before analyzing the FP effect, it is necessary to review the OPL.

$$\text{OPL} = n \times d, \tag{3}$$

where n is the real refractive index of the medium through which light travels and d represents the thickness of the object. Based on the OPL, phase Φ is expressed by the following equation:

$$\Phi = 2\pi \frac{\text{OPL}}{\lambda}. \tag{4}$$

From Eqs. (3) and (4), we can understand that the phase change is affected by the refractive index or thickness, or both. For the F-P interference approach to the modeled device, we discussed wavelength-dependent power transmission and reflection.

$$T_{FP}\lambda = \frac{1 - R_1 R_2{}^2}{1 - \zeta R_1 R_2{}^2 + 4\zeta R_1 R_2 \sin^2\varphi/2},$$
$$R_{FP}\lambda = \frac{1 - \zeta R_1 R_2{}^2 - 1 - R_1 R_2{}^2 + 4\zeta R_1 R_2 \sin^2\varphi/2}{1 - \zeta R_1 R_2{}^2 + 4\zeta R_1 R_2 \sin^2\varphi/2}, \tag{5}$$

where R_1 and R_2 denote the power reflectivity of the two mirrors that form the F-P cavity, φ denotes the roundtrip phase shift of the cavity, and $\zeta < 1$ denotes the power loss of each reflection upon the mirror, which can be caused by surface light scattering or absorption. Based on the FP resonance, the resonance wavelength in the cavity at normal incidence, this condition can be expressed as [25]

$$h = \frac{\lambda}{2n}\left(q + \frac{\varphi}{2\pi}\right), \tag{6}$$

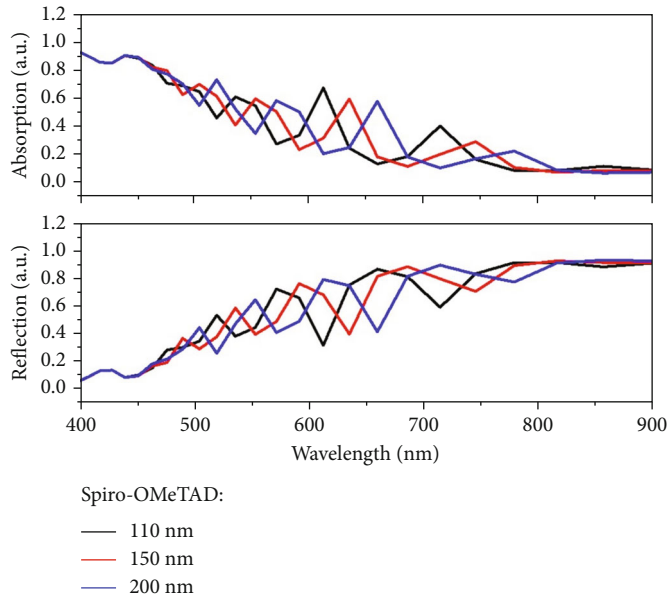

FIGURE 7: Optical performance of absorption layer within $Cs_2AgBiBr_6$ double perovskite-based solar cell with different spiro-OMeTAD layer thicknesses under solar light plane wave illumination. Top data indicate the absorption of designed architecture, and bottom data indicate the reflection of designed architecture.

where h represents the total thickness of the cavity, n represents the real refractive index in the cavity, q represents the order of the resonance, and φ denotes the phase that occurred by reflection at both interfaces of the cavity.

4. Results and Discussion

4.1. Analysis of $Cs_2AgBiBr_6$ Double Perovskite-Based Architecture. Figures 2(a)–2(d) illustrate the optical performance spectra of $Cs_2AgBiBr_6$ double perovskite-based architecture under plane wave source illumination with 400–900 nm wavelength of light. Each top data indicates the optical performance of the $Cs_2AgBiBr_6$ double perovskite-based architecture without an Au electrode (W/O Au electrode), and each bottom data indicates the optical performance of the $Cs_2AgBiBr_6$ double perovskite-based architecture with an Au electrode (W/ electrode) during the step 1 design process. Focusing on the W/O Au electrode conditions, light absorption can be calculated using the following equation: $A(\lambda) = 1 - R(\lambda) - T(\lambda)$, where $R(\lambda)$ and $T(\lambda)$ represent the reflection and transmission of the architecture, respectively. As the thickness of $Cs_2AgBiBr_6$ double perovskite layer increases, the absorption spectrum showing a narrow absorption peak in the wavelength region of approximately 430 nm broadens to the wavelength region of 660 nm. Substituting this result into the transmission calculation, almost zero transmission was exhibited in the shorter-wavelength regime light; however, the transmission increased as the longer-wavelength regime light propagated into the absorption layer. As the thickness of the absorption layer increases, the transmitted light also decreased in the shorter-wavelength light regime. In the case of reflection, the spectrum is nearly identical to the FTO reflection spectrum; however, it exhibited a value close to zero in the wavelength regime of 400–500 nm, because light absorption is high in this regime, and light is barely reflected due to the optical properties of the $Cs_2AgBiBr_6$ double perovskite. As shown in Figure 2, the reflection differs depending on the absorption layer thickness, because of the phase difference depending on the layer thickness [48]. As light absorption increased, light transmission decreased correspondingly. After forming the Au electrode on the absorption layer, the absorption spectrum became broader and enhanced, with several peaks affected by the F-P effect. The absorption enhancement over the wavelength regime can be described as the Beer–Lambert effect and cavity effect [49, 50]. For the wavelength regime of less than 500 nm, due to the Beer–Lambert effect, light absorption is dominated by thickness-dependent properties. Above the 780 nm regime, the light absorption of the architecture becomes dominated by the cavity effect. From 500 to 780 nm regimes, the architecture is affected by both effects. For the W/ Au electrode architecture, light transmission calculations were not performed; therefore, light absorption can be calculated using the following equation: $A = 1 - R$, unlike W/O electrode architecture. We quantitatively summarize the average optical performance of the W/O Au electrode-based architecture until 660 nm continuous wavelength light in Table 1. Compared with the W/O Au electrode condition, light absorption increased with the formation of the Au electrode, and light reflection by the Au electrode was calculated higher than that of the W/O Au electrode condition.

4.2. Analysis of TiO_2 Electron Transport Layer Formed in $Cs_2AgBiBr_6$ Double Perovskite-Based Architecture. In the previous simulation, we confirmed that the 600 nm absorption layer thickness exhibited the best absorption properties. Based on this result, we formed a TiO_2 layer between the FTO electrode and $Cs_2AgBiBr_6$ double perovskite absorption layer, scaling the thickness of the TiO_2 layer, and examined the optical and electrical properties. Figure 3 illustrates the

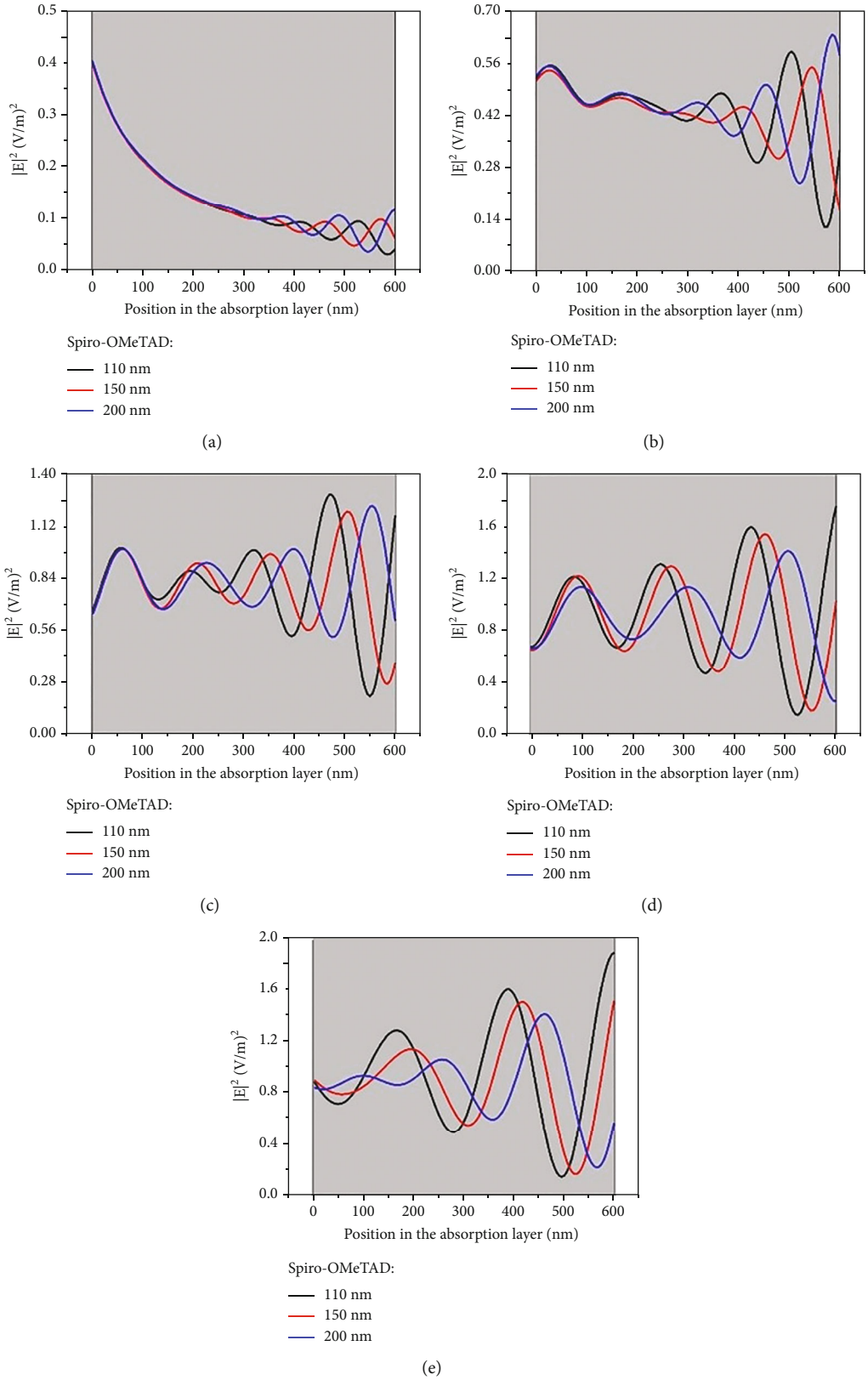

Figure 8: Spatial distribution of $|E|^2$ of absorption layer within $Cs_2AgBiBr_6$ double perovskite-based architecture with different spiro-OMeTAD layer thicknesses under solar light plane wave illumination. (a) Under 400–500 nm wavelength light illumination. (b) Under 500–600 nm. (c) Under 600–700 nm. (d) Under 700–800 nm. (e) Under 800–900 nm. The black, red, and blue spectra indicate the $|E|^2$ of the $Cs_2AgBiBr_6$ double perovskite-based architecture with 110 nm, 150 nm, and 200 nm thickness of spiro-OMeTAD layer, respectively.

Table 3: Average $|E|^2$ of the designed architecture with different spiro-OMeTAD layer thicknesses. Units are unified as $(V/m)^2$.

Spiro-OMeTAD layer thickness (nm)	Wavelength regime (nm)				
	400–500	500–600	600–700	700–800	800–900
110	0.138	0.42	0.805	0.933	0.948
150	0.14	0.43	0.792	0.895	0.883
200	0.144	0.447	0.828	0.903	0.86

$J_{sc,max}$ of the designed architecture with different TiO_2 layer thicknesses performed in step 2. For a TiO_2 layer with a thickness of 20 nm, $J_{sc,max}$ was calculated to be 13.76 mA/cm^2. However, when the TiO_2 layer thickness was increased to 40 nm, $J_{sc,max}$ dropped sharply. The architecture exhibited the lowest $J_{sc,max}$ of 13.54 mA/cm^2 when the TiO_2 layer thickness was 40 nm. As the TiO_2 layer thickness became 60 nm, $J_{sc,max}$ increased again, and at 100 nm, the maximum $J_{sc,max}$ was calculated as 13.91 mA/cm^2. Based on this result, we examined the optical performance of the absorption layer in the designed architecture. As shown in Figure 4, the optical performance showed resonance peaks, and peak appearance is different depending on the TiO_2 layer thickness. For an in-depth study of the degree of absorption for the thickness of the TiO_2 layer, we analyzed the $|E|^2$ based on Figure 4. Figure 5 shows the $|E|^2$ according to wavelength until 900 nm within the absorption layer of the architecture. The wavelength interval was divided into 100 nm, and Figures 5(a)–5(e) indicate 400–500, 500–600, 600–700, 700–800, and 800–900 nm wavelength of light, respectively. It showed the $|E|^2$ distribution in the $Cs_2AgBiBr_6$ perovskite layer with different three thicknesses of TiO_2 layers. Black, red, and blue spectra indicate the $|E|^2$ distribution of 40 nm, 100 nm, and 160 nm thickness of TiO_2 layer, respectively. When lights of each wavelength regime were illuminated to the architecture, the waveforms were different according to the thickness, which corresponded to the absorption spectra in Figure 4. The optical performance change according to the electron transport layer (ETL) thickness can be attributed to the light transmission change between the FTO/TiO_2 layer and the $Cs_2AgBiBr_6$ perovskite layer interface [51, 52]. The average $|E|^2$ of each architecture were quantitatively summarized in Table 2.

4.3. Analysis of Spiro-OMeTAD Hole Transport Layer Formed in TiO_2/$Cs_2AgBiBr_6$ Double Perovskite-Based Architecture. Previously, we completed the device optimization of the TiO_2 layer and $Cs_2AgBiBr_6$ perovskite-based architecture via FDTD simulation. Based on this, we investigated the electrical and optical properties of the spiro-OMeTAD hole transport layer (HTL). Figure 6 shows the J_{sc} variation of the device according to spiro-OMeTAD layer thickness. At a thickness of 200 nm, the $J_{sc,max}$ of the device was calculated to be a maximum value of 14.57 mA/cm^2. As the spiro-OMeTAD layer thickness increased from 20 to 200 nm, unlike the TiO_2 layer modulation process, J_{sc} continuously increased with slightly decreased characteristics. Next, we confirmed how the spiro-OMeTAD layer thickness affects the optical–electrical characteristics through absorption and average $|E|^2$ distribution. Wavelength regime conditions of step 3 are the same as step 2, and the thicknesses of the spiro-OMeTAD layer were analyzed with 110, 150, and 200 nm, representatively. Figure 7 illustrates the absorption under each wavelength light in the designed device according to different spiro-OMeTAD layer thicknesses. These values appeared in black, red, and blue lines, respectively. As the thickness of the spiro-OMeTAD layer is different, the wavelength regime where the absorption peaks appear is different. Then, the average $|E|^2$ distribution depending on the position in the absorption layer is calculated by using the transfer matrix method. Figures 8(a)–8(e) show the result of $|E|^2$ distribution within the absorption layer according to specific spiro-OMeTAD layer thicknesses under the 400–500, 500–600, 600–700, 700–800, and 800–900 nm wavelengths of light, respectively. The black, red, and blue spectra indicated the spiro-OMeTAD layer thickness with 110, 150, and 200 nm, respectively. Just as average $|E|^2$ distribution changes depending on the thickness of the TiO_2 layer, it can be confirmed that the $|E|^2$ distribution also varies depending on the thickness of spiro-OMeTAD. However, the change in the spiro-OMeTAD layer thickness led to a larger change in average $|E|^2$ distribution than the change in the TiO_2 layer thickness variation. This result indicates that the spiro-OMeTAD layer between the absorption layer and

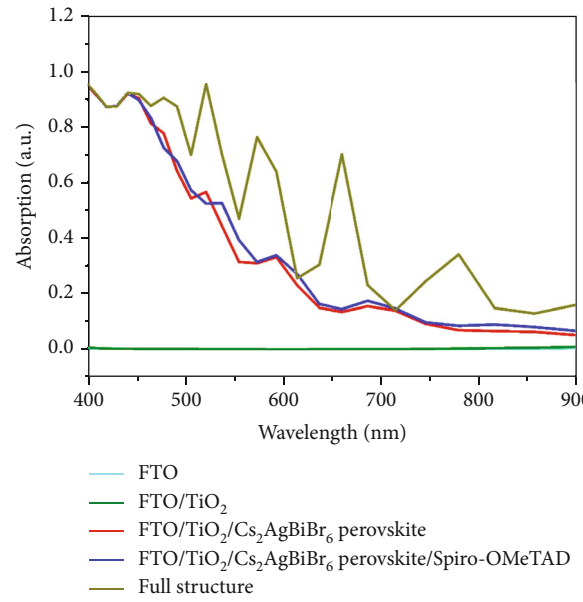

Figure 9: Absorption spectra enhancement by layer-by-layer formation.

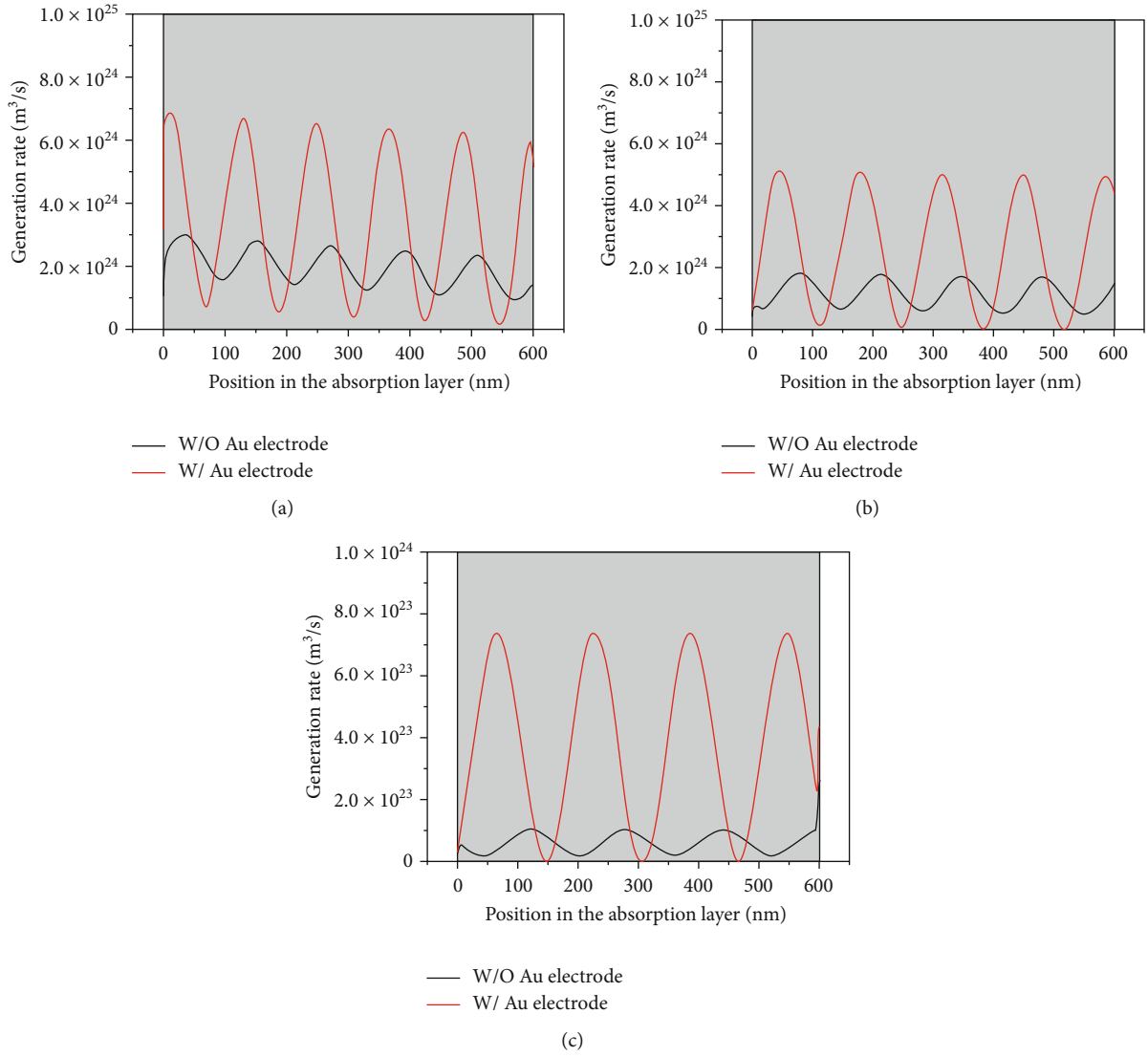

Figure 10: Charge carrier generation rate at different positions within the absorption layer of a $Cs_2AgBiBr_6$ double perovskite-based solar cell under the different monochromatic lights. (a) 520 nm, (b) 572 nm, and (c) 620 nm. Black and red spectra indicate the charge generation distribution within the absorption layer without and with Au electrode, respectively.

Au played a more crucial role as an optical space layer than the TiO_2 layer between the FTO electrode and absorption layer [53–55]. The average $|E|^2$ of each architecture according to spiro-OMeTAD layer thickness were quantitatively summarized in Table 3.

Thus far, we have investigated the performance change of $Cs_2AgBiBr_6$ PSCs through layer thickness modulation. Figures 9 and 10 depict the additive optical–electrical performances of the device under optimal conditions. As shown in Figure 9, light absorption improved accordingly as additional layers are formed. Note that numerous peaks appear in the absorption spectrum when the Au reflector is formed at the full structure. By forming the optical spacer layer, multiple reflections were involved, resulting in resonances within the device [56]. As shown in Figure 9, the resonance peaks appeared under the monochromatic lights of 520, 572, 659, and 778 nm. Based on this result, we examined the generation rate for each absorption peak. The generation rate of the architecture was calculated with and without Au electrode. Focusing on the monochromatic light of 520, 572, and 659 nm, the generation rates were distributed within the absorption layer with different positions. As shown in Figure 10, the generation rate in the absorption layer showed a higher value when forming the Au electrode. Back Au

Table 4: Maximum generation rate for each resonance peak within the absorption layer of device.

Resonance peak (nm)	Maximum generation rate	
	W/O Au electrode	W/ Au electrode
520	3.0×10^{24}	6.8×10^{24}
572	1.9×10^{24}	5.1×10^{24}
659	2.7×10^{23}	7.4×10^{23}

electrode contact provides much higher generation rate within the absorption layer associated with the FP effect. The wavelength of the illuminating light is longer, and the lower generation rate was calculated. At monochromatic light of 778 nm, it was confirmed that no charge generation occurred in the absorption layer. We quantitatively summarize the maximum generation rate for each resonance peak in the absorption layer of the device in Table 4.

5. Conclusion

In summary, in-depth analysis of optical–electrical properties influenced by the F-P effect of $Cs_2AgBiBr_6$ PSCs was performed using the FDTD method. In the FTO/$Cs_2AgBiBr_6$ perovskite/Au architecture, the OPL of the $Cs_2AgBiBr_6$ perovskite was modulated to determine the wavelength regime where resonance occurred, and the intensity or the number of resonances increased as the OPL increased. Subsequently, going through steps 2 and 3, the change in optical–electrical characteristics according to the modulation of the OPL in the TiO_2 layer or spiro-OMeTAD layer was analyzed by calculating the J_{sc}, absorption, and average $|E|^2$. Finally, we investigated the resonance peaks according to the optimization of the device and analyzed the distribution of the generation rate according to the peaks in each wavelength region. This insight is meaningful in predicting the F-P effect that occurs theoretically by scaling the layer thickness of conventional n-i-p perovskite solar cells, which are commonly addressed, and provides the guideline for optical modeling in the fabrication of real nanosized standard photovoltaics.

Data Availability

The data used to support the findings of this study are included within the supplementary information file(s).

Conflicts of Interest

All authors declare that they have no conflicts of interest.

Acknowledgments

This work was partly supported by the innovative Human Resource Development for Local Intellectualization program through the Institute of Information & Communications Technology Planning & Evaluation (IITP) grant funded by the Korea government (MSIT) (IITP-2024-RS-2022-00156389, 50%) and the National Research Foundation of Korea (NRF) grant funded by the Korean government (MSIT) (2021R1A2C1011429, 50%).

Supplementary Materials

Figure S1: complex refractive index of each material. Black spectra indicate the real part, and blue spectra indicate the extinction coefficient part. The complex refractive index of FTO, $Cs_2AgBiBr_6$, and spiro-OMeTAD referred to literature, and TiO_2 and Au referred to Siefke and CRC which are embedded in the Lumerical FDTD software, respectively. *(Supplementary Materials)*

References

[1] A. Mostafaeipour, M. Jahangiri, H. Saghaei, A. Raiesi Goojani, M. S. Chowdhury, and K. Techato, "Impact of different solar trackers on hydrogen production: a case study in Iran," *International Journal of Photoenergy*, vol. 2022, Article ID 3186287, 15 pages, 2022.

[2] N. Kannan and D. Vakeesan, "Solar energy for future world: - a review," *Renewable and Sustainable Energy Reviews*, vol. 62, pp. 1092–1105, 2016.

[3] M. Jahangiri, M. Rezaei, A. Mostafaeipour et al., "Prioritization of solar electricity and hydrogen co-production stations considering PV losses and different types of solar trackers: a TOPSIS approach," *Renewable Energy*, vol. 186, pp. 889–903, 2022.

[4] S. Sun, M. Xu, Y. Zhang et al., "Study of molybdenum oxide optimized hole carrier transport in perovskite solar cells," *Organic Electronics*, vol. 113, article 106697, 2023.

[5] J. Park, J. Kim, H.-S. Yun et al., "Controlled growth of perovskite layers with volatile alkylammonium chlorides," *Nature*, vol. 616, no. 7958, pp. 724–730, 2023.

[6] J. Ramanujam and U. P. Singh, "Copper indium gallium selenide based solar cells – a review," *Energy & Environmental Science*, vol. 10, no. 6, pp. 1306–1319, 2017.

[7] L. Qiu, S. He, L. K. Ono, and Y. Qi, "Progress of surface science studies on ABX_3-based metal halide perovskite solar cells," *Advanced Energy Materials*, vol. 10, no. 13, article 1902726, 2019.

[8] C. Wu, Q. Zhang, Y. Liu et al., "The dawn of lead-free perovskite solar cells: highly stable double perovskite $Cs_2AgBiBr_6$ film," *Advancement of Science*, vol. 5, no. 3, article 1700759, 2017.

[9] X.-G. Zhao, J.-H. Yang, Y. Fu et al., "Design of lead-free inorganic halide perovskites for solar cells via cation-transmutation," *Journal of the American Chemical Society*, vol. 139, no. 7, pp. 2630–2638, 2017.

[10] N. Ding, L. Shao, T. Xie et al., "Highly-sensitive, stable, and fast response lead-free $Cs_2AgBiBr_6$ double perovskite photodetectors enabled by synergistic engineering of doping Na^+/Ce^{3+} and integrating ag nanoparticles film," *Laser & Photonics Reviews*, vol. 16, no. 12, article 220031, 2022.

[11] G. Longo, S. Mahesh, L. R. Buizza et al., "Understanding the performance-limiting factors of $Cs_2AgBiBr_6$ double-perovskite solar cells," *ACS Energy Letters*, vol. 5, no. 7, pp. 2200–2207, 2020.

[12] M. Zhai, C. Chen, and M. Cheng, "Advancing lead-free $Cs_2AgBiBr_6$ perovskite solar cells: challenges and strategies," *Solar Energy*, vol. 253, pp. 563–583, 2023.

[13] I. Spanopoulos, W. Ke, and M. G. Kanatzidis, "In quest of environmentally stable perovskite solar cells: a perspective," *Helvetica Chimica Acta*, vol. 104, no. 1, article e2000173, 2021.

[14] R. L. Hoye, L. Eyre, F. Wei et al., "Fundamental carrier lifetime exceeding 1 μs in $Cs_2AgBiBr_6$ double perovskite," *Advanced Materials Interfaces*, vol. 5, no. 15, article 1800464, 2018.

[15] C. F. Guo, T. Sun, F. Cao, Q. Liu, and Z. Ren, "Metallic nanostructures for light trapping in energy-harvesting devices," *Light: Science & Applications*, vol. 3, no. 4, article e161, 2014.

[16] R. S. Dubey and V. Ganesan, "Fabrication and characterization of TiO_2/SiO_2 based Bragg reflectors for light trapping applications," *Results in Physics*, vol. 7, pp. 2271–2276, 2017.

[17] C.-Y. Huang, D.-Y. Wang, C.-H. Wang et al., "Efficient light harvesting by photon downconversion and light trapping in

hybrid ZnS nanoparticles/Si nanotips solar cells," *ACS Nano*, vol. 4, no. 10, pp. 5849–5854, 2010.

[18] A. Mellor, N. P. Hylton, S. A. Maier, and N. Ekins-Daukes, "Interstitial light-trapping design for multi-junction solar cells," *Solar Energy Materials and Solar Cells*, vol. 159, pp. 212–218, 2017.

[19] P. J. Maake, A. S. Bolokang, C. J. Arendse, V. Vohra, E. I. Iwuoha, and D. E. Motaung, "Metal oxides and noble metals application in organic solar cells," *Solar Energy*, vol. 207, pp. 347–366, 2020.

[20] M. Laska, Z. Krzemińska, K. Kluczyk-Korch et al., "Metallization of solar cells, exciton channel of plasmon photovoltaic effect in perovskite cells," *Nano Energy*, vol. 75, article 104751, 2020.

[21] I. Ullah, H. Saghaei, J. Khan, and S. K. Shah, "The role of plasmonic metal-oxides core-shell nanoparticles on the optical absorption of perovskite solar cells," *Optical and Quantum Electronics*, vol. 54, no. 10, p. 675, 2022.

[22] A. A. Tabrizi, H. Saghaei, M. A. Mehranpour, and M. Jahangiri, "Enhancement of absorption and effectiveness of a perovskite thin-film solar cell embedded with gold nanospheres," *Plasmonics*, vol. 16, no. 3, pp. 747–760, 2021.

[23] B. Sun, L. Zhao, C. Wang et al., "Tunable Fano resonance in E-shape plasmonic nanocavities," *Journal of Physical Chemistry C*, vol. 118, no. 43, pp. 25124–25131, 2014.

[24] L. Bai, J. Liu, Y. Tang et al., "Synergistic enhancements in the performances of dye-sensitized solar cells by the scattering and plasmon resonance of Au-nanoparticle multi-shell hollow nanospheres," *International Journal of Energy Research*, vol. 44, no. 8, pp. 7026–7034, 2020.

[25] P. Li, X. Jiang, S. Huang, Y. Lu, and N. Fu, "Plasmonic perovskite solar cells: an overview from metal particle structure to device design," *Surfaces and Interfaces*, vol. 25, article 101287, 2021.

[26] X. D. Zhang, Y. Zhao, Y. T. Gao et al., "Influence of front electrode and back reflector electrode on the performances of microcrystalline silicon solar cells," *Journal of Non-Crystalline Solids*, vol. 352, no. 9-20, pp. 1863–1867, 2006.

[27] H. R. Yeom, J. Heo, G.-H. Kim et al., "Optimal top electrodes for inverted polymer solar cells," *Physical Chemistry Chemical Physics*, vol. 17, no. 3, pp. 2152–2159, 2015.

[28] L. Yang, Y. Xuan, and J. Tan, "Efficient optical absorption in thin-film solar cells," *Optics Express*, vol. 19, no. S5, article A1165, 2011.

[29] Z. Djurić and I. Jokić, "Ideal efficiency of resonant cavity-enhanced perovskite solar cells," *Optical and Quantum Electronics*, vol. 52, pp. 1–8, 2020.

[30] S. Bae, M. Duff, J. Y. Hong, and J.-K. Lee, "Optical engineering of PbS colloidal quantum dot solar cells via Fabry-Perot resonance and distributed Bragg reflectors," *Nano Convergence*, vol. 10, no. 1, p. 31, 2023.

[31] N. Vandamme, H.-L. Chen, A. Gaucher et al., "Ultrathin GaAs solar cells with a silver back mirror," *IEEE Journal of Photovoltaics*, vol. 5, no. 2, pp. 565–570, 2015.

[32] R. Ren, Y. Guo, and R. Zhu, "Design of a plasmonic back reflector for silicon nanowire decorated solar cells," *Optics Letters*, vol. 37, no. 20, pp. 4245–4247, 2012.

[33] X. Sheng, J. Liu, I. Kozinsky, A. M. Agarwal, J. Michel, and L. C. Kimering, "Design and non-lithographic fabrication of light trapping structures for thin film silicon solar cells," *Advanced Materials*, vol. 23, no. 7, pp. 843–847, 2011.

[34] E. Massa, V. Giannini, N. P. Hylton et al., "Diffractive interference design using front and rear surface metal and dielectric nanoparticle arrays for photocurrent enhancement in thin crystalline silicon solar cells," *ACS Photonics*, vol. 1, no. 9, pp. 871–877, 2014.

[35] R. Sen and M. Yadav, "Performance Analysis of Lead-Free Perovskite Solar Cells," in *Topical Drifts in Intelligent Computing. ICCTA 2021*, J. K. Mandal, P. A. Hsiung, and R. Sankar Dhar, Eds., vol. 426 of Lecture Notes in Networks and Systems, Springer, Singapore, 2022.

[36] J. George, A. P. Joseph, and M. Balachandran, "Perovskites: emergence of highly efficient third-generation solar cells," *International Journal of Energy Research*, vol. 46, no. 15, pp. 21856–21883, 2022.

[37] J. H. Kim, L. Chrostowski, E. Bisaillon, and D. V. Plant, "DBR, Sub-wavelength grating, and Photonic crystal slab Fabry-Perot cavity design using phase analysis by FDTD," *Optics Express*, vol. 15, no. 16, pp. 10330–10339, 2007.

[38] Y. A. Pritom, D. K. Sikder, S. Zaman, and M. Hossain, "Plasmon-enhanced parabolic nanostructures for broadband absorption in ultra-thin crystalline Si solar cells," *Nanoscale Advances*, vol. 5, no. 18, pp. 4986–4995, 2023.

[39] H. Lu, W. Tian, B. Gu, Y. Zhu, and L. Li, "TiO2electron transport bilayer for highly efficient planar perovskite solar cell," *Small*, vol. 13, no. 38, article 1701535, 2017.

[40] Q. Lou, G. Lou, H. Guo et al., "Enhanced efficiency and stability of n-i-p perovskite solar cells by incorporation of fluorinated graphene in the spiro-OMeTAD hole transport layer," *Advanced Energy Materials*, vol. 12, no. 36, article 2201344, 2022.

[41] Y. Hao, T. Ailing, and A. Asundi, "Challenges of digital holography in micro-optical measurement," in *Proceedings Volume 7522, Fourth International Conference on Experimental Mechanics*, vol. 752249, Singapore, Singapore, 2010.

[42] A. Taflove and S. C. Hagness, "Finite-difference time-domain solution of Maxwell's equations," *Wiley Encyclopedia of Electrical and Electronics Engineering*, pp. 1–33, 2016.

[43] A. Didari-Bader and H. Saghaei, "Penrose tiling-inspired graphene-covered multiband terahertz metamaterial absorbers," *Optics Express*, vol. 31, no. 8, pp. 12653–12668, 2023.

[44] M. T. Islam, M. R. Jani, S. M. A. Amin et al., "Numerical simulation studies of a fully inorganic $Cs_2AgBiBr_6$ perovskite solar device," *Optical Materials*, vol. 105, article 109957, 2020.

[45] H. I. Elsaeedy, A. Qasem, H. A. Yakout, and M. Mahmoud, "The pivotal role of TiO_2 layer thickness in optimizing the performance of TiO_2/P-Si solar cell," *Journal of Alloys and Compounds*, vol. 867, article 159150, 2021.

[46] J. Li, J. X. Yao, X. Y. Yao et al., "A contact study in hole conductor free perovskite solar cells with low temperature processed carbon electrodes," *RSC Advances*, vol. 7, no. 34, pp. 20732–20737, 2017.

[47] A. Bag, R. Radhakrishnan, R. Nekovei, and R. Jeyakumar, "Effect of absorber layer, hole transport layer thicknesses, and its doping density on the performance of perovskite solar cells by device simulation," *Solar Energy*, vol. 196, pp. 177–182, 2020.

[48] M. K. Gunde and Z. C. Orel, "Thickness-dependent optical effects in infrared reflection-absorption spectra of a fairly thick polymer layer," *Applied Spectroscopy*, vol. 56, no. 1, pp. 24–30, 2002.

[49] M. Long, Z. Chen, T. Zhang et al., "Ultrathin efficient perovskite solar cells employing a periodic structure of a composite hole conductor for elevated plasmonic light harvesting and hole collection," *Nanoscale*, vol. 8, no. 12, pp. 6290–6299, 2016.

[50] Q. Lin, A. Armin, R. C. R. Nagiri, P. L. Burn, and P. Meredith, "Electro-optics of perovskite solar cells," *Nature Photonics*, vol. 9, no. 2, pp. 106–112, 2015.

[51] K. Huang, Y. Peng, Y. Gao et al., "High-performance flexible perovskite solar cells via precise control of electron transport layer," *Advanced Energy Materials*, vol. 9, no. 44, article 1901419, 2019.

[52] J. Feng, Z. Yang, D. Yang et al., "E-beam evaporated Nb_2O_5 as an effective electron transport layer for large flexible perovskite solar cells," *Nano Energy*, vol. 36, pp. 1–8, 2017.

[53] J. Y. Kim, P. Vincent, J. Jang et al., "Versatile use of ZnO interlayer in hybrid solar cells for self-powered near infra-red photo-detecting application," *Journal of Alloys and Compounds*, vol. 813, article 152202, 2020.

[54] C. Cho, T. Antrack, M. Kroll et al., "Electrical pumping of perovskite diodes: toward stimulated emission," *Advanced Science*, vol. 8, no. 17, article 2101663, 2021.

[55] A. Roy, S. H. Park, S. Cowan et al., "Titanium suboxide as an optical spacer in polymer solar cells," *Applied Physics Letters*, vol. 95, no. 1, article 013302, 2009.

[56] Y. Oteki, N. Miyashita, M. Giteau, K. Shiba, T. Sogabe, and Y. Okada, "Enhanced current generation in quantum-dot intermediate band solar cells through optimizing the position of quantum dot layers," *Optical Materials: X*, vol. 16, article 100207, 2022.